

On-Demand Mode Conversion and Wavefront Shaping via On-Chip Metasurfaces

Lin Deng, Yihao Xu, Renchao Jin, Ziqiang Cai, and Yongmin Liu*

In this work, mode conversion and wavefront shaping by integrating a metallic metasurface on top of a planar waveguide are proposed and demonstrated. The metasurface consists of C-shaped nanoantennas. By controlling the orientation of each nanoantenna, mode conversion and focusing effect for the cross-polarized electric fields inside the waveguide are achieved. The design and simulation results of 16 scenarios of wideband transverse-magnetic to transverse-electric mode converters with the mode purity up to 98%, and on-chip lenses at the wavelength of 1550 nm are reported. It is worth noting that the dimension of the devices along the propagation direction is only 9.6 μm . This work manifests the potential application of mode division multiplexing systems and on-chip optical interconnections based on metasurfaces.

1. Introduction

Integrated photonics that can transfer and process massive information has received extensive attention from both industry and academia because of its large information capacity, miniature footprint, complementary metal-oxide-semiconductor (CMOS) compatibility, and low power consumption.^[1–5] Specifically, the orthogonality of distinct eigenmodes coexisting in a photonic waveguide makes it possible to implement mode division multiplexing (MDM) technology, allowing various modes with different polarization states and orders to simultaneously propagate inside the waveguide. In this way, the channel number and thus the information capacity can be efficiently increased.^[6–10] The two basic components in the MDM system include mode converters and polarization rotators which can change the mode order and the polarization direction of the input guided mode,^[4,11,12] respectively. Normally, individual transverse electric (TE) and transverse magnetic (TM) modes inside a multi-mode waveguide can propagate independently without energy exchange since they are orthogonal to each other. However, in the presence

of external perturbation, controllable mode conversion with polarization change can be implemented. Recently, several methods have been proposed to achieve this goal. For example, waveguides with asymmetric cross-sections,^[13–18] including L shape and double-stair shape, as well as asymmetric metallic cover layers,^[19–21] can break the orthogonality of TE₀ and TM₀ mode and hence produce direct conversion between them. Such devices can function as polarization rotators, since the input and output modes always share the same mode order but with different polarization directions. Another method for polarization manipulation is based on mode evolution, where a mode hybridization region is used to

gradually convert the input mode into the orthogonal polarization with the same or higher order.^[11,22] However, this strategy requires a large length of the mode hybridization region up to hundreds of micrometers because it should satisfy the adiabatic transition condition.

Metasurfaces, which are made up of an array of artificial sub-wavelength structures to locally manipulate the amplitude, phase, and polarization of light, represent one frontier in photonics research.^[23–32] Based on elaborately designed metasurfaces, novel applications such as holographic image display,^[33–41] imaging with meta-lenses,^[42–47] orbital angular momentum (OAM) beam generation,^[48–53] and polarization manipulation^[54–59] have been demonstrated. However, most of these metasurfaces operate in free space, and the entire systems still consist of bulky optical components including light sources, mirrors, polarizers, etc. To further reduce the overall size and complexity, researchers have recently investigated the hybrid platform by integrating metasurfaces with photonic waveguides that preserve the merits of each system. Applications like mode converters, polarization rotators, second-harmonic generation, on-chip wavefront shaping and OAM lasers have been reported.^[60–67] With the assistance of metasurfaces, the wavevector of the guided mode can be modified and the mode coupling coefficient can be optimized, ensuring the efficient conversion from the fundamental mode to higher-order mode. On the other hand, 2D phase shaping of the input planar waveguide mode was realized by deliberately controlling the local phase or refractive index with metasurfaces.^[66,68,69] However, to the best of our knowledge, a universal and straightforward method for arbitrarily converting TM modes to TE modes or wavefront shaping for the cross-polarized waves is still lacking.

In this paper, we propose a new design strategy for mode converters and polarization rotators utilizing on-chip C-shaped

L. Deng, Z. Cai, Y. Liu
Department of Electrical and Computer Engineering
Northeastern University
Boston, MA 02115, USA
E-mail: y.liu@northeastern.edu

Y. Xu, R. Jin, Y. Liu
Department of Mechanical and Industrial Engineering
Northeastern University
Boston, MA 02115, USA

 The ORCID identification number(s) for the author(s) of this article can be found under <https://doi.org/10.1002/adom.202200910>.

DOI: 10.1002/adom.202200910

plasmonic nanostructures, which support pronounced electric and magnetic resonances. Compared to the previous methods that convert the fundamental TE mode to other modes by modifying the wavenumbers of guided modes while considering the mode profiles of the input/target modes as well as the near-field components of the nanoantenna, our design can directly generate the required wavefront of the desired TE modes from various TM modes. In addition, the phase tuning range for the co-polarized field component of the waveguide modes using the nano-bar structure is from 0 to π .^[63–65] In contrast, the phase change of our C-shape nanoantenna can cover the entire 2π range, which is beneficial to implement high-order cross-polarization mode conversion and other practical applications. Finally, we demonstrate on-chip lenses that can shrink the spot size while rotating the polarization direction of the input waveguide mode with a footprint of $9.6\ \mu\text{m}$ along the propagation direction. To the best of our knowledge, it is the first demonstration of simultaneous polarization rotation and wavefront shaping for photonic waveguide mode using on-chip metasurfaces.

2. Results and Discussions

Figure 1a shows the schematic of our first device, where the gold C-shaped nanostructures with different rotation angles are placed on top of a multi-mode Ta_2O_5 waveguide. Ta_2O_5 , Si_3N_4 , and LiNbO_3 have been widely used in integrated photonics for their CMOS compatibility, low loss, and high nonlinear effect.^[70–74] Compared to silicon, these materials have lower

refractive indexes, so the strong interaction between the waveguide modes and the metasurfaces can ensure the efficient mode and polarization conversion process. Please note that our proposed method could be potentially applied to the silicon platform with modified parameters including the size and the period of the C-shaped nanoantennas. These nanostructures can interact with the evanescent wave components of the waveguide modes, allowing us to manipulate the waveguide modes. After passing through the metasurface region, the input TM modes (i.e., TM_0 , TM_1 , TM_2 , and TM_3) can be converted to the TE modes (i.e., TE_0 , TE_1 , TE_2 , and TE_3), giving rise to the total possible conversion combinations of 16. For each scenario, one set of metasurfaces with the ability to engineer the local phase of the generated E_y component is designed and integrated on the waveguide. Instead of providing the additional wave vectors, our metasurfaces directly generate the phases required for the cross-polarized field component while depleting the input TM modes through the interaction between the metasurfaces and the evanescent wave components of waveguide modes. This property makes our design suitable for complicated situations, for instance, when the input and output modes have very close wavenumber or large mode numbers. Figure 1b illustrates the designed function of our second device, in which a focal point with dominant E_y component is generated at the right side of the metasurface under TM_0 mode incidence. The design follows the same approach as mode conversion since the phase profile of the generated E_y component can be modified for a predefined function, which is the focusing function in this case.

A schematic of the gold C-shaped nanoantenna in our metasurfaces is shown in the inset at the top left corner of Figure 2a.

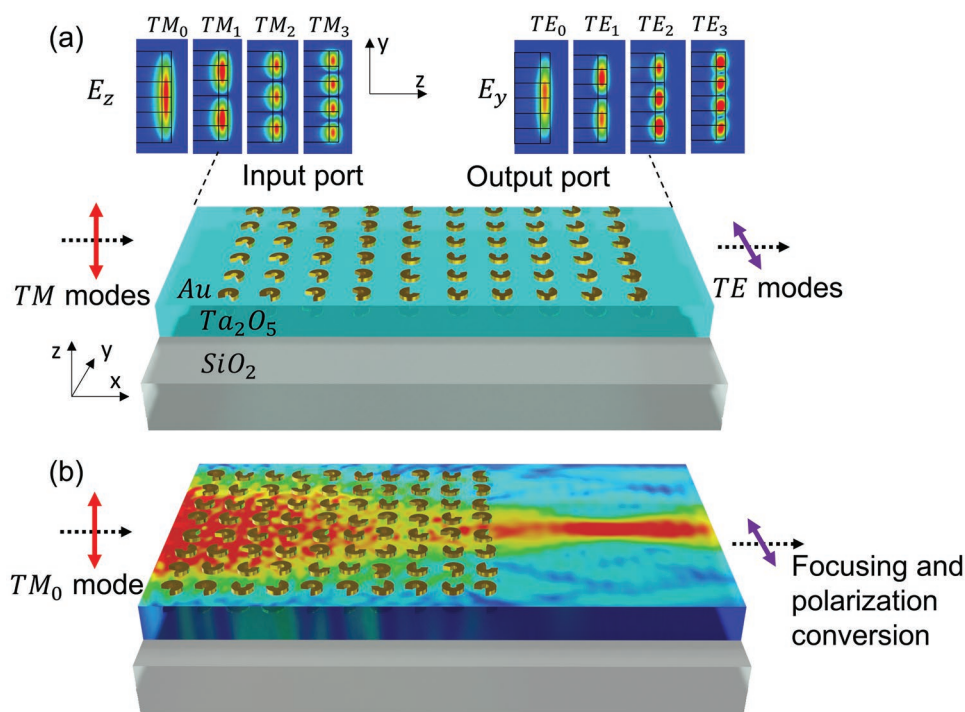


Figure 1. a) Schematic of mode conversion via on-chip metasurfaces. The insets on the top represent the simulated TM and TE mode profile at the input and output ports, respectively. b) Schematic of a 2D lens that can generate a focal point along with polarization conversion for TM_0 mode incidence.

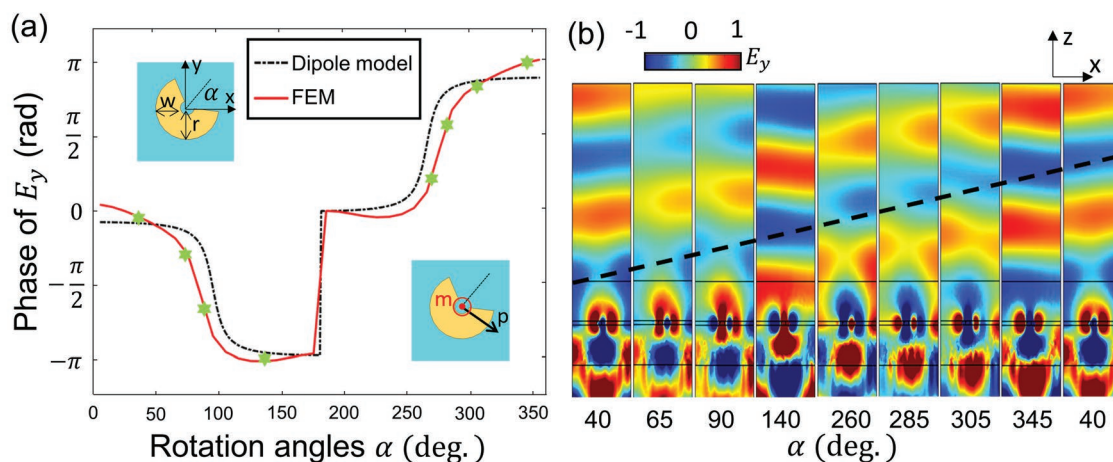


Figure 2. a) Dependence of the phase of the scattered E_y field on the rotation angle of C-shaped nanoantenna, when the input is a TM mode. The black line and red line represent the results obtained from the dipole model and FEM simulation, respectively. The insets show the geometry, as well as the electric dipole (p) and magnetic dipole (m) modes of the C-shaped nanoantenna. b) The field distribution of E_y component for the eight rotation angles marked as the star symbols in (a).

For each nanoantenna, the rotation angle is defined as α with respect to the horizontal direction (i.e., x -axis), while the opening angle, width and radius are denoted as θ , w , and r , respectively. COMSOL Multiphysics, a commercial electromagnetic solver based on the finite element method (FEM), is used to evaluate the dependence of the phase on the rotation angle. In the simulation of a single unit cell, one C-shaped nanoantenna with opening angle $\theta = 120^\circ$, width $w = 90$ nm, radius $r = 125$ nm, and thickness $t = 40$ nm is placed on top of a 400 nm-thick Ta_2O_5 dielectric waveguide. The refractive index of Ta_2O_5 is 2.06 at 1550 nm wavelength. TM modes are input from the left port. By rotating the structure from 0° to 360° , the phase of the scattered E_y component can cover the whole 2π range as shown in Figure 2a. The relation between the phase change and the rotation angle is attributed to the dipole modes, as illustrated in the inset at the bottom right corner of Figure 2a. The C-shaped nanoantenna can support a strong in-plane electric dipole mode perpendicular to the symmetric axis and an out-of-plane magnetic mode along the z -direction.^[75,76] The TM input mode contains three evanescent wave components, that is, H_y , E_x , and E_z , outside the waveguide. The electric component E_x can induce the in-plane electric dipole mode. Then the excited electric field can be further decomposed to the y -direction, given by $E_{y1} \propto E_x \sin(\alpha) \cos(\alpha)$. In addition, the input E_x component can excite the magnetic dipole m_z , which would in turn generate another E_{y2} component given by $E_{y2} \propto E_x \sin(\alpha)$. The phase retardations between these E_{y1} and E_{y2} should also be considered in our model. Consequently, the final form of the generated electric field E_y can be expressed as follows with four fitting parameters:

$$E_y = E_{y1} + E_{y2} = \sin(\alpha) e^{i\phi} (E_1 \cos(\alpha) + E_2 e^{i\gamma}) \quad (1)$$

As shown in Figure 2a, our dipole model matches the simulated phase profile reasonably well, with the fitting parameters $E_1 = 1$, $E_2 = 0.15$, $\phi = 0.7\pi$, and $\gamma = 1.7\pi$. In Figure 2b we plot the generated electric field E_y for eight selected rotation angles (denoted by the star symbols in Figure 2a). The simulated results clearly show the linear phase gradient indicated by the

black dotted line, along which all of the electric field E_y of the eight structures share the same phase.

Since we can generate cross-polarized scattered light with the phase covering the entire 2π range, the wavefront of the scattered light can be modified in a prescribed manner. For any input TM modes and output TE modes, we can always extract their phase profiles at the cross-section inside the waveguide. The phase difference can be compensated by the C-shaped nanoantenna with appropriate rotation angles. As a proof-of-principle demonstration, we have considered three different scenarios including TM_0 to TE_0 , TM_0 to TE_3 , and TM_1 to TE_2 mode conversions, which are shown in Figure 3. Since the C-shape nanoantennas are placed periodically on the top of the waveguide, the continuous phase profiles of the input and target modes can be further simplified as discrete values in the grid where the nanoantennas are patterned. Moreover, in order to avoid the back-reflection inside the waveguide, the period of the unit cell p should meet the requirement of $p \neq \frac{\lambda}{n_{\text{TE}}}$ and $p \neq \frac{\lambda}{n_{\text{TM}}}$, where λ is 1550 nm, and n_{TE} and n_{TM} stand for the effective refractive index of the TE and TM mode, respectively. The height and width of the Ta_2O_5 channel waveguide is fixed at 400 nm and is 4.8 μm , respectively. The effective refractive indices for the waveguide modes from TE_0 to TE_3 are 1.71, 1.69, 1.65, and 1.60, and the effective mode indexes for the waveguide modes from TM_0 to TM_3 are 1.56, 1.54, 1.50, and 1.45, respectively. The period along the propagation direction is chosen to be 640 nm, while the period perpendicular to the propagation direction is chosen to be 400 nm. For the first case shown in Figure 3a, both of the input and output modes are fundamental modes, and the only difference in their phase profile is due to the different wavenumbers. Therefore, the additional phase profile to implement the mode conversion, which is calculated by subtracting the input phase profile from the output phase profile, should have the same value along the y -direction. The phase profile in Figure 3b,c is more complicated because higher-order modes are involved. However, it is still straightforward to retrieve the additional phase profiles and thus the

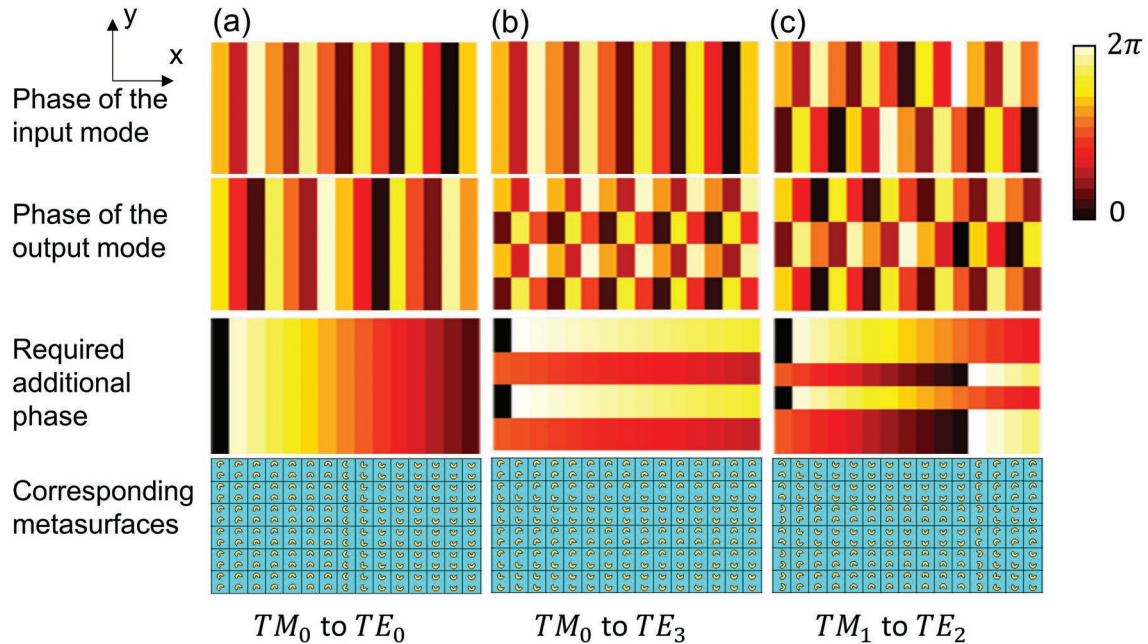


Figure 3. Mode conversion for three cases: a) TM_0 to TE_0 , b) TM_0 to TE_3 , and c) TM_1 to TE_2 . In each column, the panels from top to bottom show the discrete phase profile for 1) the input mode, 2) the output mode, 3) the additional phase provided by the metasurfaces to compensate the phase mismatch, and 4) the designed metasurfaces for each case.

orientations of individual C-shaped nanoantennas. The reason for setting the period along y -direction as 400 nm is because 12 unit cells can be equally spaced for the planar waveguide with a width of 4.8 μm , and 12 is the least common multiple of 1, 2, 3, and 4. In order to maximize the ratio of the generated TE mode to the residual TM mode, the column number of antennas along the propagation direction is set as 15 in all simulations. Therefore, the overall functional area of our on-chip metasurfaces is 9.6 $\mu\text{m} \times 4.8 \mu\text{m}$. In the last step, based on the

required additional phase profiles and the results in Figure 2a, we can determine the rotation angle of the C-shaped nanoantenna in each unit cell as shown in the bottom row in Figure 3.

The simulation of the TM_1 to TE_2 mode conversion was performed by CST Studio Suite, a commercial electromagnetic solver. From top to bottom, the three figures in Figure 4a show the electric field E_z of the input TM_1 mode, the integrated metasurface, and the electric field E_y of the generated TE_2 mode, respectively. When passing through the metasurface region,

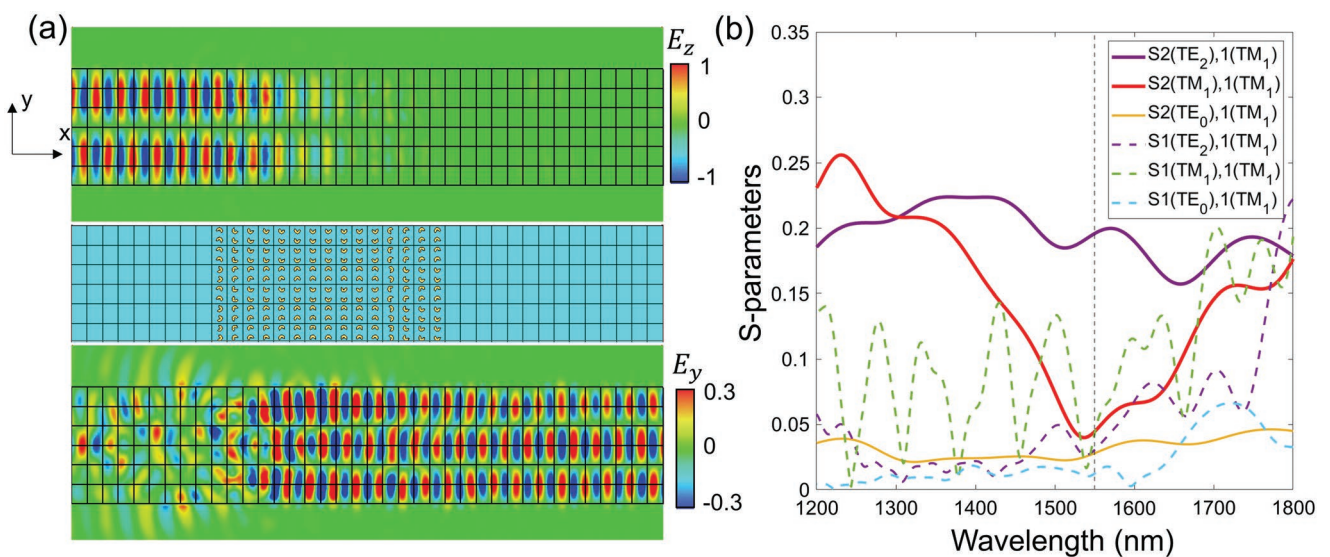


Figure 4. a) Field profile of the input TM_1 modes (top) and the generated TE_2 mode (bottom), as well as the corresponding on-chip metasurfaces (middle). b) Simulated S-parameters of the mode converter. The vertical dashed line indicates 1550 nm wavelength.

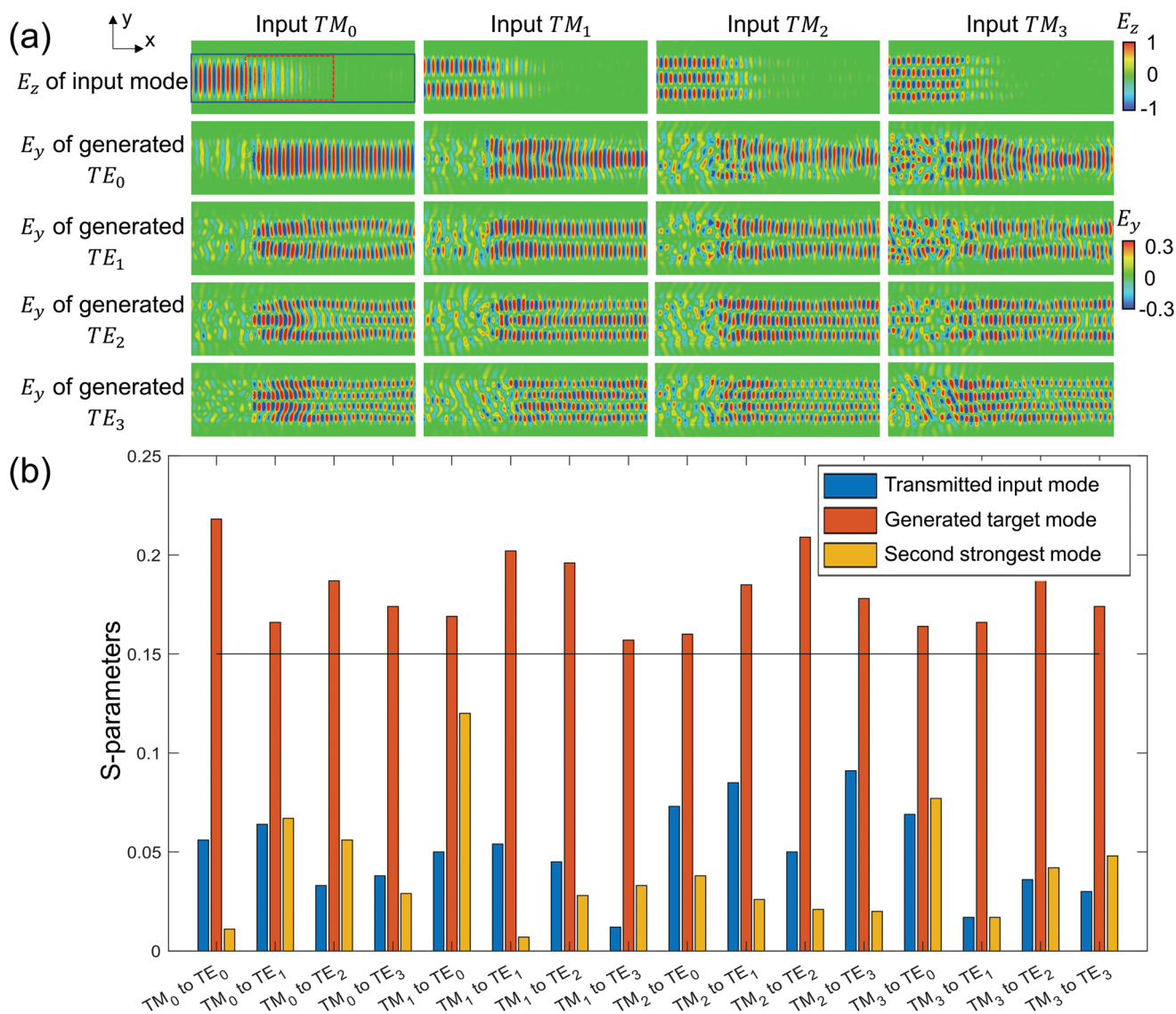


Figure 5. a) Electric fields of the input modes and the generated modes inside the waveguide for 16 scenarios. The red dash box and the black box denote the regions of the metasurfaces and waveguide, respectively. b) S-parameters for the transmitted input modes, generated target modes, and the second strongest generated modes.

the input TM_1 mode gradually dissipates while a uniform TE_2 mode emerges at the same time. Besides the energy exchange of the two modes, there are other reasons for the dissipation of the TM mode: First, compared to TE modes, TM modes suffer from higher ohmic losses during the propagation for their stronger interaction with the metallic structure.^[77,78] In addition, the C-shaped nanoantenna is designed to resonate with the TM mode at the working wavelength, so that it would strongly interact with the evanescent wave of the input mode. The calculated S-parameter further confirms the performance of the device. As shown in Figure 4b, $S_2(TE_2)_1(TM_1)$, which represents the normalized field amplitude of the generated TE_2 mode with respect to the incident TM_1 mode, reaches 0.195, while $S_2(TM_1)_1(TM_1)$, which represents the normalized amplitude of the transmitted TM_1 mode, drops to a very low value of 0.045. Owing to the field profile mismatch of the two modes,

other modes, such as TE_0 , could be generated while the conversion efficiency is low (for example, $S_2(TE_0)_1(TM_1)$ is around 0.04). Meanwhile, the backscattering at 1550 nm is weak as evidenced by the S_{11} parameters. We define the working bandwidth as the wavelength range in which the target mode purity is greater than 90%. Then the working bandwidth is around 70 nm for the TM_1 to TE_2 mode conversion case, which can benefit the further expansion of the optical communication channels by wavelength division multiplexing techniques.

To have an overall picture of the mode converter, we simulated the electric field distribution inside the waveguide for all of the 16 TM-TE mode conversions at 1550 nm wavelength. The results are plotted in Figure 5a. The first row shows the E_z components, which can also indicate any residual TM fields. The second to fifth rows depict the E_y components of the generated TE modes. The black box represents the waveguide region and

the red box denotes the location of the metasurfaces as shown in the top left figure. S-parameters of the 16 scenarios in Figure 5b quantify the mode conversion results in detail. As shown in the diagram, the S-parameters of the generated target modes are always between 0.16 and 0.22 while the S-parameters of the input modes are reduced to 0.02–0.08. Although the intensity mismatches between the input modes and target modes cause the generation of unwanted modes indicated by the S-parameter of the second strongest generated modes and the imperfect mode profiles of E_y component, they always exhibit much lower intensities compared to the designed modes. With a mode conversion length of $9.6 \mu\text{m}$ for all 16 situations, our metasurfaces are capable of generating the desired TE modes with high purity ranging from 63% to 98%, as shown in Figure S1 (Supporting Information). The purity of mode is defined as the ratio of the target output mode power to the total transmitted power.^[61] Our C-shaped metasurface shows the advantages of simple designs for the high-order mode conversion, high mode purity, wideband response, and small footprint. The detailed comparison between our work and literature is summarized in Table S1 (Supporting Information). Moreover, the maximum bandwidth we find in our simulation is around 150 nm for the TM_0 to TE_0 case, which can be found in Figure S2 (Supporting Information). Please note that the geometric parameters of the aforementioned metasurfaces are set as $\theta = 120^\circ$, $w = 90 \text{ nm}$, and $r = 125 \text{ nm}$ to make sure they can resonate at around 1550 nm, so that the transmitted input mode can be dramatically suppressed. By modifying the geometries of the C-shaped antenna to tune its resonant wavelength away from 1550 nm, for example, changing the radius to 110 nm, the amplitude of the residual input modes and the target modes could become comparable as shown in Figure S3 (Supporting Information). This kind of configuration can potentially benefit the MDM technique considering the coexisting and propagation of two orthogonal waveguide modes.

Different from the mode conversion process, where only phase or wavenumber change is involved, wavefront shaping needs more complicated and precise control of the local phases. There are published works that use metasurfaces and metamaterials to realize wavefront shaping, including focusing and mode size conversion, for the co-polarized electric field.^[66,68,69] However, wavefront shaping for cross-polarized light, which would potentially benefit the MDM system and optical interconnection, is much less explored. Considering that our metasurfaces can control the phase of the E_y component generated by TM mode incidence, in the following we will demonstrate an in-plane focusing lens for the cross-polarized light. The phase profile of the focusing lens needs to satisfy:

$$\frac{2\pi}{\lambda} n_{\text{eff}} \left(\sqrt{(x_f - x_i)^2 + (y_f - y_i)^2} \right) + \phi_i(x, y) = 2m\pi \quad (2)$$

Here x_f and y_f are the coordinate of the focal point and x_i and y_i are the coordinate of the i th unit cell. n_{eff} is the effective refractive index of the generated E_y component and λ is the working wavelength. The additional phase needed for each location is ϕ_i , and m is an integer. We first consider that the focal point is located at $(3.2, 0) \mu\text{m}$. As shown in Figure 6a, 15×15 unit cells with a total area of $9.6 \times 9.6 \mu\text{m}^2$ are placed on the top of the planar waveguide. Figure 6b present the the electric field amplitude inside the waveguide, from which we can observe a focal point exactly at the designed location and the field is E_y dominant. The field amplitude at the focal point is comparable to that of the input TM mode. The phase and amplitude profile of the generated E_y component in Figure 6c,d further confirms that the wavefront shaping is achieved by controlling the local phase via the metasurface. Since the input TM_0 mode can be focused to the TE_0 mode with a much narrower width along the transverse direction, we can use a ridge waveguide with the width of $0.64 \mu\text{m}$ to pick up this TE mode (see Figure S4, Supporting Information). The average amplitude of the generated

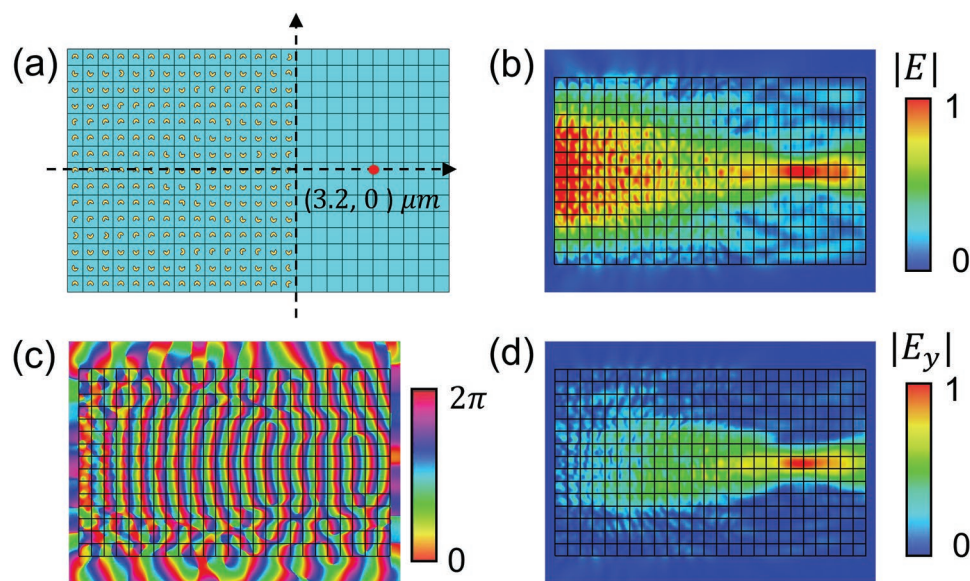


Figure 6. a) Schematic of the proposed on-chip lens and the location of the focal point. b) Amplitude profile of E inside the waveguide. c,d) Phase and amplitude profile of the generated E_y component.

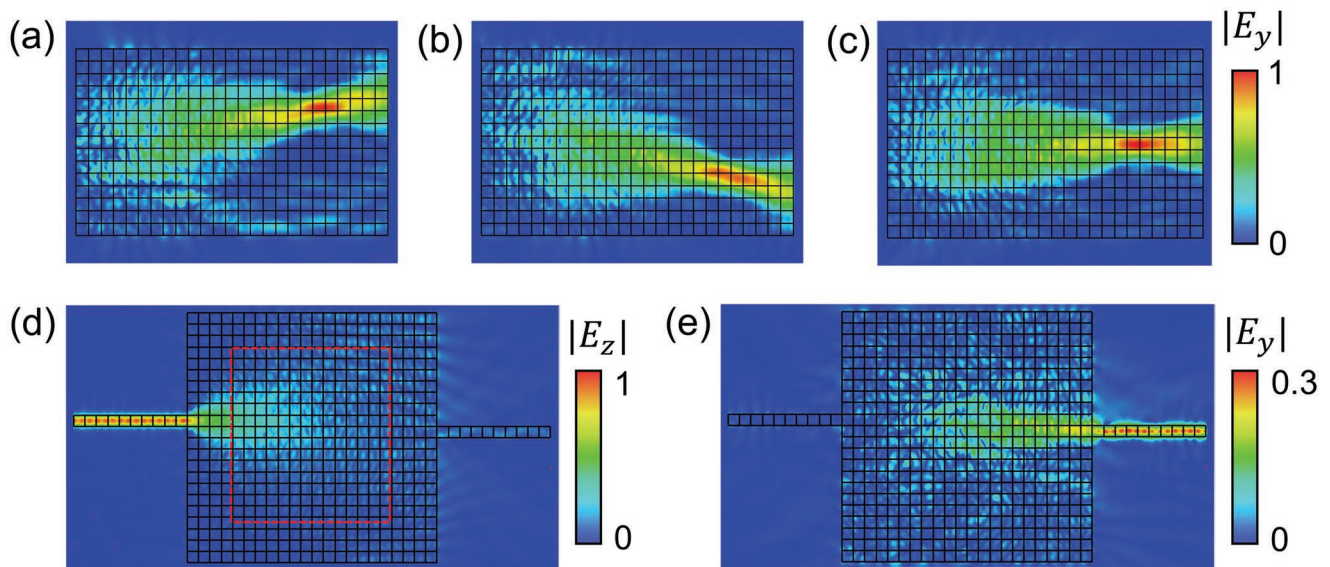


Figure 7. a–c) Amplitude profiles of E_y inside the waveguide for three different focal points. d,e) Amplitude profiles of E_z and E_y when the metasurfaces in the red box are designed to convert the scattered light with E_z component to TE mode at the output port.

TE_0 mode is almost the same as the input amplitude while the corresponding S_{21} parameter is around 0.22. Moreover, since the local phase of each unit cell can be readily controlled, we can focus the E_y component at specified positions as shown in Figure 7a–c, where the focal points are designed at $(3.2, 1.92)$ μm , $(3.2, -1.92)$ μm , and $(3.2, 0)$ μm , respectively, using the same coordinate as Figure 6. In addition to the normal slab waveguide mode, when the TM mode is input from a thin waveguide and diverges in the planar waveguide region as shown in Figure 7d,e, our design can also allow us to funnel light to a thin waveguide port on the right. The metasurface (outlined by the red box) can convert the light to E_y polarization and focus it on the output port as TE mode with the S_{21} parameter around 0.19. The 0.64 μm offset of the input port and output port along the vertical direction also shows the flexibility of our design. The specific metasurface designs used in Figure 7a–d can be found in Figure S5 (Supporting Information).

3. Conclusion

In conclusion, we propose and demonstrate an innovative method for wideband mode conversion and wavefront shaping, when the input guided mode is TM polarized. The rotation of the polarization and tuning of the local phase are achieved through the interaction between the on-chip metasurfaces and evanescent wave components of waveguide modes. With appropriately designed metasurfaces, our devices can realize the generation of the target modes with high purity and accurate control of the focal points. Furthermore, we can apply our approach to infrared and THz systems, given the scalability of Maxwell's equations. We envision that our concept may inspire novel applications such as MDM, on-chip optical interconnection and computation, optical router, and light detection and ranging devices.

Supporting Information

Supporting Information is available from the Wiley Online Library or from the author.

Acknowledgements

Y.L. acknowledges the financial support from the National Science Foundation (ECCS-2136168 and ECCS-1916839).

Conflict of Interest

The authors declare no conflict of interest.

Data Availability Statement

The data that support the findings of this study are available from the corresponding author upon reasonable request.

Keywords

integrated photonics, metasurfaces, mode conversion, wavefront shaping

Received: April 19, 2022

Revised: July 29, 2022

Published online:

- [1] R. Soref, *IEEE J. Sel. Top. Quantum Electron.* **2006**, *12*, 1678.
- [2] R. Soref, *Nat. Photonics* **2010**, *4*, 495.
- [3] A. H. Atabaki, S. Moazeni, F. Pavanello, H. Gevorgyan, J. Notaros, L. Alloatti, M. T. Wade, C. Sun, S. A. Kruger, H. Meng, *Nature* **2018**, *556*, 349.
- [4] M. Teng, A. Honardoost, Y. Alahmadi, S. S. Polkoo, K. Kojima, H. Wen, C. K. Renshaw, P. LiKamWa, G. Li, S. Fathpour, *J. Lightwave Technol.* **2020**, *38*, 6.

- [5] M. He, M. Xu, Y. Ren, J. Jian, Z. Ruan, Y. Xu, S. Gao, S. Sun, X. Wen, L. Zhou, *Nat. Photonics* **2019**, *13*, 359.
- [6] D. Dai, C. Li, S. Wang, H. Wu, Y. Shi, Z. Wu, S. Gao, T. Dai, H. Yu, H. K. Tsang, *Laser Photonics Rev.* **2018**, *12*, 1700109.
- [7] D. Richardson, J. Fini, L. E. Nelson, *Nat. Photonics* **2013**, *7*, 354.
- [8] P. J. Winzer, *Nat. Photonics* **2014**, *8*, 345.
- [9] L.-W. Luo, N. Ophir, C. P. Chen, L. H. Gabrielli, C. B. Poitras, K. Bergmen, M. Lipson, *Nat. Commun.* **2014**, *5*, 3069.
- [10] C. Li, D. Liu, D. Dai, *Nanophotonics* **2018**, *8*, 227.
- [11] D. Dai, Y. Tang, J. E. Bowers, *Opt. Express* **2012**, *20*, 13425.
- [12] W. Chang, L. Lu, X. Ren, D. Li, Z. Pan, M. Cheng, D. Liu, M. Zhang, *Opt. Express* **2018**, *26*, 8162.
- [13] Z. Wang, D. Dai, *J. Opt. Soc. Am. B* **2008**, *25*, 747.
- [14] A. Xie, L. Zhou, J. Chen, X. Li, *Opt. Express* **2015**, *23*, 3960.
- [15] K. Goi, A. Oka, H. Kusaka, K. Ogawa, T.-Y. Liow, X. Tu, G.-Q. Lo, D.-L. Kwong, *Opt. Lett.* **2015**, *40*, 1410.
- [16] L. Chen, C. R. Doerr, Y.-K. Chen, *Opt. Lett.* **2011**, *36*, 469.
- [17] W. Ye, X. Yuan, Y. Gao, J. Liu, *Opt. Express* **2017**, *25*, 33176.
- [18] J. Zhang, M. Yu, G.-Q. Lo, D.-L. Kwong, *IEEE J. Sel. Top. Quantum Electron.* **2009**, *16*, 53.
- [19] J. Zhang, S. Zhu, H. Zhang, S. Chen, G.-Q. Lo, D.-L. Kwong, *IEEE Photonics Technol. Lett.* **2011**, *23*, 1606.
- [20] M.-a. Komatsu, K. Saitoh, M. Koshiba, *IEEE Photonics J.* **2012**, *4*, 707.
- [21] L. Gao, Y. Huo, J. S. Harris, Z. Zhou, *IEEE Photonics Technol. Lett.* **2013**, *25*, 2081.
- [22] D. Chen, X. Xiao, L. Wang, W. Liu, Q. Yang, S. Yu, *Opt. Lett.* **2016**, *41*, 1070.
- [23] N. Yu, F. Capasso, *Nat. Mater.* **2014**, *13*, 139.
- [24] A. V. Kildishev, A. Boltasseva, V. M. Shalaev, *Science* **2013**, *339*, 1232009.
- [25] B. Xiong, L. Deng, R. Peng, Y. Liu, *Nanoscale Adv.* **2019**, *1*, 3786.
- [26] N. Meinzer, W. L. Barnes, I. R. Hooper, *Nat. Photonics* **2014**, *8*, 889.
- [27] N. M. Estakhri, A. Alu, *Phys. Rev. X* **2016**, *6*, 041008.
- [28] S. Jahani, Z. Jacob, *Nat. Nanotechnol.* **2016**, *11*, 23.
- [29] L. Huang, S. Zhang, T. Zentgraf, *Nanophotonics* **2018**, *7*, 1169.
- [30] X. Ni, N. K. Emami, A. V. Kildishev, A. Boltasseva, V. M. Shalaev, *Science* **2012**, *335*, 427.
- [31] S. Chen, Z. Li, W. Liu, H. Cheng, J. Tian, *Adv. Mater.* **2019**, *31*, 1802458.
- [32] F. Z. Shu, J. N. Wang, R. W. Peng, B. Xiong, R. H. Fan, Y. J. Gao, Y. Liu, D. X. Qi, M. Wang, *Laser Photonics Rev.* **2021**, *15*, 2100155.
- [33] L. Jin, Z. Dong, S. Mei, Y. F. Yu, Z. Wei, Z. Pan, S. D. Rezaei, X. Li, A. I. Kuznetsov, Y. S. Kivshar, *Nano Lett.* **2018**, *18*, 8016.
- [34] G. Yoon, D. Lee, K. T. Nam, J. Rho, *ACS Nano* **2018**, *12*, 6421.
- [35] J. Li, S. Kamin, G. Zheng, F. Neubrech, S. Zhang, N. Liu, *Sci. Adv.* **2018**, *4*, 6768.
- [36] S. C. Malek, H.-S. Ee, R. Agarwal, *Nano Lett.* **2017**, *17*, 3641.
- [37] S. M. Kamali, E. Arbabi, A. Arbabi, Y. Horie, M. Faraji-Dana, A. Faraon, *Phys. Rev. X* **2017**, *7*, 041056.
- [38] B. Wang, F. Dong, Q.-T. Li, D. Yang, C. Sun, J. Chen, Z. Song, L. Xu, W. Chu, Y.-F. Xiao, *Nano Lett.* **2016**, *16*, 5235.
- [39] D. Wen, F. Yue, G. Li, G. Zheng, K. Chan, S. Chen, M. Chen, K. F. Li, P. W. H. Wong, K. W. Cheah, *Nat. Commun.* **2015**, *6*, 8241.
- [40] B. Xiong, Y. Xu, J. Wang, L. Li, L. Deng, F. Cheng, R. W. Peng, M. Wang, Y. Liu, *Adv. Mater.* **2021**, *33*, 2005864.
- [41] W. Ma, Y. Xu, B. Xiong, L. Deng, R.-W. Peng, M. Wang, Y. Liu, *Adv. Mater.* **2022**, *34*, 2110022.
- [42] M. Khorasaninejad, F. Capasso, *Science* **2017**, *358*, 8100.
- [43] M. Khorasaninejad, W. T. Chen, R. C. Devlin, J. Oh, A. Y. Zhu, F. Capasso, *Science* **2016**, *352*, 1190.
- [44] S. Wang, P. C. Wu, V.-C. Su, Y.-C. Lai, M.-K. Chen, H. Y. Kuo, B. H. Chen, Y. H. Chen, T.-T. Huang, J.-H. Wang, *Nat. Nanotechnol.* **2018**, *13*, 227.
- [45] S. Wang, P. C. Wu, V.-C. Su, Y.-C. Lai, C. H. Chu, J.-W. Chen, S.-H. Lu, J. Chen, B. Xu, C.-H. Kuan, *Nat. Commun.* **2017**, *8*, 187.
- [46] M. Khorasaninejad, F. Aieta, P. Kanhaiya, M. A. Kats, P. Genevet, D. Rousso, F. Capasso, *Nano Lett.* **2015**, *15*, 5358.
- [47] R. Jin, L. Tang, J. Li, J. Wang, Q. Wang, Y. Liu, Z.-G. Dong, *ACS Photonics* **2020**, *7*, 512.
- [48] F. Yue, D. Wen, J. Xin, B. D. Gerardot, J. Li, X. Chen, *ACS Photonics* **2016**, *3*, 1558.
- [49] N. Yu, P. Genevet, M. A. Kats, F. Aieta, J.-P. Tetienne, F. Capasso, Z. Gaburro, *Science* **2011**, *334*, 333.
- [50] X. Ma, M. Pu, X. Li, C. Huang, Y. Wang, W. Pan, B. Zhao, J. Cui, C. Wang, Z. Zhao, *Sci. Rep.* **2015**, *5*, 10365.
- [51] J. Jin, M. Pu, Y. Wang, X. Li, X. Ma, J. Luo, Z. Zhao, P. Gao, X. Luo, *Adv. Mater. Technol.* **2017**, *2*, 1600201.
- [52] X. Zang, Y. Zhu, C. Mao, W. Xu, H. Ding, J. Xie, Q. Cheng, L. Chen, Y. Peng, Q. Hu, *Adv. Opt. Mater.* **2019**, *7*, 1801328.
- [53] J. Han, Y. Intaravanne, A. Ma, R. Wang, S. Li, Z. Li, S. Chen, J. Li, X. Chen, *Laser Photonics Rev.* **2020**, *14*, 2000146.
- [54] H. Wang, L. Shi, B. Lukyanchuk, C. Sheppard, C. T. Chong, *Nat. Photonics* **2008**, *2*, 501.
- [55] J. Li, S. Chen, H. Yang, J. Li, P. Yu, H. Cheng, C. Gu, H. T. Chen, J. Tian, *Adv. Funct. Mater.* **2015**, *25*, 704.
- [56] A. I. Kuznetsov, A. E. Miroshnichenko, M. L. Brongersma, Y. S. Kivshar, B. Luk'yanchuk, *Science* **2016**, *354*, 2472.
- [57] R. Zhao, L. Huang, C. Tang, J. Li, X. Li, Y. Wang, T. Zentgraf, *Adv. Opt. Mater.* **2018**, *6*, 1800490.
- [58] Q. Yang, M. Liu, S. Kruk, Y. Xu, Y. K. Srivastava, R. Singh, J. Han, Y. Kivshar, I. V. Shadrivov, *Adv. Opt. Mater.* **2020**, *8*, 2000555.
- [59] L. Kang, S. P. Rodrigues, M. Taghinejad, S. Lan, K.-T. Lee, Y. Liu, D. H. Werner, A. Urbas, W. Cai, *Nano Lett.* **2017**, *17*, 7102.
- [60] D. Ohana, U. Levy, *Opt. Express* **2014**, *22*, 27617.
- [61] D. Ohana, B. Desiatov, N. Mazurski, U. Levy, *Nano Lett.* **2016**, *16*, 7956.
- [62] H. Wang, Y. Zhang, Y. He, Q. Zhu, L. Sun, Y. Su, *Adv. Opt. Mater.* **2019**, *7*, 1801191.
- [63] Z. Li, M.-H. Kim, C. Wang, Z. Han, S. Shrestha, A. C. Overvig, M. Lu, A. Stein, A. M. Agarwal, M. Lončar, N. Yu, *Nat. Nanotechnol.* **2017**, *12*, 675.
- [64] C. Wu, H. Yu, S. Lee, R. Peng, I. Takeuchi, M. Li, *Nat. Commun.* **2021**, *12*, 96.
- [65] C. Wang, Z. Li, M.-H. Kim, X. Xiong, X.-F. Ren, G.-C. Guo, N. Yu, M. Lončar, *Nat. Commun.* **2017**, *8*, 2098.
- [66] Z. Wang, T. Li, A. Soman, D. Mao, T. Kananen, T. Gu, *Nat. Commun.* **2019**, *10*, 3547.
- [67] X. Guo, Y. Ding, X. Chen, Y. Duan, X. Ni, *Sci. Adv.* **2020**, *6*, 4142.
- [68] U. Levy, M. Abashin, K. Ikeda, A. Krishnamoorthy, J. Cunningham, Y. Fainman, *Phys. Rev. Lett.* **2007**, *98*, 243901.
- [69] Y. Fan, X. Le Roux, A. Korovin, A. Lupu, A. de Lustrac, *ACS Nano* **2017**, *11*, 4599.
- [70] M. Belt, M. L. Davenport, J. E. Bowers, D. J. Blumenthal, *Optica* **2017**, *4*, 532.
- [71] Q. Zhao, R. O. Behunin, P. T. Rakich, N. Chauhan, A. Isichenko, J. Wang, C. Hoyt, C. Fertig, M. h. Lin, D. J. Blumenthal, *APL Photonics* **2020**, *5*, 116103.
- [72] T. Doumuki, H. Tamada, M. Saitoh, *Appl. Phys. Lett.* **1994**, *65*, 2519.
- [73] X. Han, Y. Jiang, A. Frigg, H. Xiao, P. Zhang, T. G. Nguyen, A. Boes, J. Yang, G. Ren, Y. Su, *Laser Photonics Rev.* **2022**, *16*, 2100529.
- [74] A. Billat, D. Grassani, M. H. Pfeiffer, S. Kharitonov, T. J. Kippenberg, C.-S. Brès, *Nat. Commun.* **2017**, *8*, 1016.
- [75] Z. Wang, K. Yao, M. Chen, H. Chen, Y. Liu, *Phys. Rev. Lett.* **2016**, *117*, 157401.
- [76] L. Li, K. Yao, Z. Wang, Y. Liu, *Laser Photonics Rev.* **2020**, 1900244.
- [77] J. T. Kim, J. J. Ju, S. Park, M.-s. Kim, S. K. Park, S.-Y. Shin, *Opt. Express* **2010**, *18*, 2808.
- [78] P. D. Flammer, J. M. Banks, T. E. Furtak, C. G. Durfee, R. E. Hollingsworth, R. T. Collins, *Opt. Express* **2010**, *18*, 21013.